Applied Thermal Engineering 290 (2026) 130125

Contents lists available at ScienceDirect

Applied Thermal Engineering

journal homepage: www.elsevier.com/locate/apthermeng

Research Paper

Thermoelectric generators for harvesting medium-temperature geothermal anomalies: *printed* vs *bulk devices*

Muhammad Irfan Khan [a,*], Leonard Franke [a,b], Andres Georg Rösch [a], Zirui Wang [a], Md. Mofasser Mallick [a,b], Patricia Alegría [c], Nerea Pascual [c], David Astrain [c], Uli Lemmer [a,d,e]

[a] Light Technology Institute, Karlsruhe Institute of Technology (KIT), 76131 Karlsruhe, Germany
[b] Varmo UG (haftungsbeschränkt), Alter Schlachthof 39, 76131 Karlsruhe, Germany
[c] Department of Engineering, Public University of Navarre (UPNA), 31006 Pamplona, Spain
[d] InnovationLab GmbH, Speyerer Strasse 4, 69115 Heidelberg, Germany
[e] Institute of Microstructure Technology, Karlsruhe Institute of Technology (KIT), Hermann-von-Helmholtz-Platz 1, 76344 Eggenstein-Leopoldshafen, Germany

ARTICLE INFO

Keywords:
Thermoelectric generators
Printed thermoelectrics
Geothermal anomalies
Thermosyphon

ABSTRACT

Recently, thermoelectric generators (TEGs) have gained significant attention for directly converting geothermal energy into electricity. Due to the considerable variations in heat-source and sink geometries and boundary conditions, the design of TEGs should offer flexibility to fulfill the specific constraints. Printing technologies, such as screen printing or 3D printing, offer versatile, cost-effective manufacturing approaches for TEGs, enabling scalability and shape conformability. In this work, we present a comparative performance optimization of both printed TEGs and bulk-material-based TEGs for medium-temperature geothermal anomalies at T ~ 170 °C. The proposed system for geothermal energy harvesting consists of a two-phase thermosyphon serving as the hot-side heat exchanger, TEGs, and an efficient heat sink based on heat pipes. We investigate the performance of both types of TEGs attached to the exterior of the thermosyphon for three heights (h = 100, 200, and 500 mm). For both bulk and printed TEGs, thermal and electrical impedance optimizations are achieved by adjusting the TEG fill factor, leg dimensions, and the cross-sectional areas of the n-type and p-type legs. Under the given boundary conditions, the higher power density at lower cost occurs at a TEG height of 100 mm for both bulk and printed-TEG devices. And in all three cases, at a higher fill factor ($F \sim 0.9$), printed TEGs showed comparable power densities to bulk TEGs at lower cost. As F decreases, the printed TEGs' power densities drop more rapidly than those of their bulk counterparts. Despite lower performance at lower fill factors, printed TEGs remain promising, with lower cost per watt (€/W) thanks to lower TE material consumption and lower manufacturing cost. Lastly, the projection of the levelized cost of electricity LCOE (€/kWh) and the economic analysis for both approaches conclude our work.

1. Introduction

The rising global energy demands and regulatory obligations to mitigate greenhouse gas have resulted in prioritizing sustainable and renewable energy over conventional ones [1]. In addition to solar, wind, bio, and hydropower, geothermal energy ranks among the most promising renewable resources due to its abundance and minimal environmental footprint. Among these, geothermal energy stands out due to its stability, high availability factor (~80%), and independence from time and weather [2,3]. These attributes allow geothermal plants to operate at a higher capacity factor, ultimately generating more electricity than equivalent plants operating on intermittent renewable energy resources. The importance of geothermal energy in confronting environmental challenges has been acknowledged for the supply of both electricity and heat, with scientific evidence confirming its role as a vital solution [4–7]. Numerous studies have been conducted emphasizing the transition to renewable energy sources [8,9], specifically the role of geothermal energy in CO_2 reduction in geothermal-rich countries [5,9].

Besides heating, electricity generation is another important aspect of geothermal energy. The Organic Rankine Cycle (ORC) is currently the main technology for generating electricity from this resource. In theory, the basic principle of an ORC is simple. Firstly, an organic liquid working fluid with a high molecular mass and a lower vaporization temperature

* Corresponding author.
E-mail address: muhammad.khan3@kit.edu (M.I. Khan).

https://doi.org/10.1016/j.applthermaleng.2026.130125
Received 9 December 2025; Received in revised form 25 January 2026; Accepted 2 February 2026
Available online 7 February 2026

Nomenclature

Symbols

d	diameter, (mm)
t	thickness, (mm)
y	depth, (mm)
h	height, (mm)
w	water level, (mm)
n_f	no. of fins
l	length, (mm)
Ψ	thermal resistance, (K/W)
$\dot{Q}$	heat flow, (W)
h_{conv}	convection HTC, (W/(m^2·K))
A	area, (m^2)
m	thermal fin parameter
T	temperature, (K)
F	fill factor
F_{ang}	angle factor
W_{cond}	conductor overlapping
Z	figure of merit (1/K)
n_{tc}	no. of thermocouples
P	power, (W)
p_d	power density, (W/m^2)
R	electrical resistance, (Ω)
I	current, (A)
V	voltage, (V)
K	TEG thermal conductance, (W/K)

Greek symbols

η	efficiency
κ	thermal conductivity, (W/(m·K))
α	seebeck coefficient, (V/K)
σ	electrical conductivity, (S/m)
Δ	difference
γ	angle

Subscripts and superscripts

f	fins
$conv$	convective
ch	characteristics
H & h	hot side
C & c	cold side
geo	geothermal
amb	ambient
int	internal
k_1 & k_2	conduction
boi	boiling
con	condensation
eff	effective
$load$	load (external)
TEG	thermoelectric generator
n	n-type
p	p-type
$safe$	safety
$total$	total
eq	equivalent
max	maximum
$cont$	contacts

than water is heated and converted into high-temperature, high-pressure vapor. The vapor is then expanded into the turbine section, generating electrical power via an attached generator. After that, the vapor is cooled and condensed, then returned to the geothermal heat source to restart the next cycle. However, an ORC has many challenges, including the need for a centralized well location, high capital and operational costs, large flow rates, and the need to manage cooling systems [10]. Also, among the various geothermal resources, one notable type is the Hot Dry Rock (HDR) field, which consists of hot impermeable rocks without any fluid or reservoir. HDR fields are estimated to represent over 99% of the total geothermal energy potential in the United States [11]. Currently, the dominant way to utilize these fields is to drill boreholes. Water is then pumped into the hot rock field and then heated, similar to a hydrothermal system [12]. This approach, however, involves creating man-made boreholes to depths of several kilometers. Unfortunately, this method may potentially induce seismic activity and could be associated with high environmental impact and low economic viability. Moreover, the existing HDR field plants are not easily adaptable to low power, as they are primarily designed to be viable only at higher power outputs [13]. To mitigate these challenges, Thermoelectric generator (TEG) technology has become a promising option for converting geothermal energy into electrical energy [14,15]. The TEGs directly convert thermal energy into electrical energy by the Seebeck effect. The key advantages of TEGs over other energy conversion technologies are: no moving parts, ensuring vibration-free operation; compactness; longer life with minimal maintenance, etc. [16]. These pros pave the way for integrating TEGs into geothermal sources by reducing operational and maintenance costs [17].

Suter et al. [18] designed and optimized a 1 kW_{el} TEG stack for geothermal power generation, simulating its geometrical and operating parameters. Liu et al. [19] constructed a TEG system for geothermal applications capable of generating 160 W of electricity at a temperature difference of 80 °C. This system consisted of 96 TEG modules with a maximum installed capacity of 500 W at a 200 °C temperature difference. They stated that this TEG system is cost-effective compared to photovoltaics (PV), considering equivalent energy generation. Ahiska and Mamur [20] conducted an experimental study on the design and implementation of a portable 100 W_{max} TEG setup for low-grade geothermal energy. They reported a generated power of 41.6 W with a TEG conversion efficiency of 3.9% at a temperature difference of 67 °C. Gholamian et al. [21] enhanced the performance of a geothermal-based ORC by proposing two distinct configurations. In the first configuration, TEGs were used to harvest waste heat and convert it into electricity, and in the second configuration, electrical power from TEGs was used to produce hydrogen in an electrolyzer. They reported that the performance of these configurations exceeded that of the basic ORC setup by 21.9% and 12.7%, respectively. Khanmohammadi et al. [22] conducted the performance and economic analysis of a TEG-integrated geothermal-based Organic Rankine flash cycle (ORFC) along with a fuel cell. Their findings demonstrated that, with TEG integration, the system's first- and second-law efficiencies increased by 2.7% and 2.8%, respectively. Ding et al. [10] conducted a theoretical study showing that segmented annular cylindrical TEGs spanning 500 m could produce 136 kW of electric power at a geothermal fluid temperature of 130 °C. They explored the effects of temperature and geothermal fluid flow rate on TEG power output. Catalan et al. [23] developed a system with two TEG modules to convert the heat in gases from fumaroles into electricity, ultimately supplying power to the volcanic monitoring stations. The system used heat pipes as the heat exchangers and produced an electric power of 0.32–0.33 W per module with a temperature range of 69–86 °C. Catalan et al. [24] also experimentally investigated a bi-phase closed thermosyphon with two TEG modules integrated outside of its condensation section to convert geothermal energy in shallow hot dry rock fields into electrical energy. They reported net power generation of 3.29 W per module at a temperature difference of 180 °C. In another study [25] by the same group, they investigated the thermoelectric energy generation potential at two different sites: a) Islote Hilario and b) Casa de los Camelleros in Timanfaya National Park (Canary Islands,

Spain). There, they estimated a potential annual electricity generation of 681.53 MWh. At these locations, extreme geothermal anomalies exist where temperatures of 100–600 °C are reached at depths of only 1–13 m. These conditions result from a shallow magmatic body that heats air in porous rocks, which then rises to the surface by natural convection. Ambient air infiltrates the porous medium, is rapidly heated in deep fractures near the magmatic source, and then rises toward the surface due to buoyancy [25,26]. Alegria et al. [27] designed a geothermal TEG (GTEG) for high temperature geothermal anomalies like in Islote Hilario, which consists of a big thermosyphon as a hot side heat exchanger and a set of several small heat pipes as a cold side heat exchanger (see Fig. 1). They determined that installing more TEG modules on this vertical thermosyphon increases cumulative power but decreases conversion efficiency per module. One GTEG (with 8 TEG modules) produced a maximum power of 36 W, generating 286.94 kWh annually. They also calculated a potential annual electricity generation of 7.24 GWh [15]. Alegria et al. [28] installed a 400 W thermoelectric generation system in an HDR field in the Canary Islands, Spain. Astrain et al. [29] installed the first passive thermoelectric generator in Antarctica, achieving an average year-round power output of 4.4 W and a total energy generation of 38 kWh annually under field conditions.

It has been widely reported that, at relatively low temperatures and flow rates, the implementation of ORC systems and other conventional energy-conversion technologies becomes challenging. This limitation arises primarily from the low-grade nature and limited exergy content of the available heat, which requires careful working-fluid selection and increasingly careful cycle design, leading to higher costs and system complexity [30,31].

In this work, we consider a geothermal anomaly located in the region named: Casa de los Camelleros (Timanfaya National Park, Lanzarote, Spain), spanning a 4000 m^2 area, as reported in Refs. [15, 26]. The field measurements in these studies indicate that the hot gases from fumaroles are consistently available with a temperature of ~170 °C at near-surface depths. However, as this heat source consists of gases with a composition similar to ambient air, it is not thermally equivalent to water/other liquid heat sources at the same temperature due to its much lower heat capacity. Consequently, conventional or complex power-generation systems are not well suited for exploiting such low-grade heat sources (c.f. Fig. 2). Therefore, for small-scale and low-maintenance power generation ranging from a few watts to several tens of watts, particularly for self-consumption facilities in remote areas, TEG technology becomes especially attractive owing to its simplicity, reliability, and ability to operate effectively under these conditions [32]. Accordingly, in the present study, hot gases ~170 °C are utilized as the heat source to generate electrical energy using a two-phase closed thermosyphon integrated with TEGs.

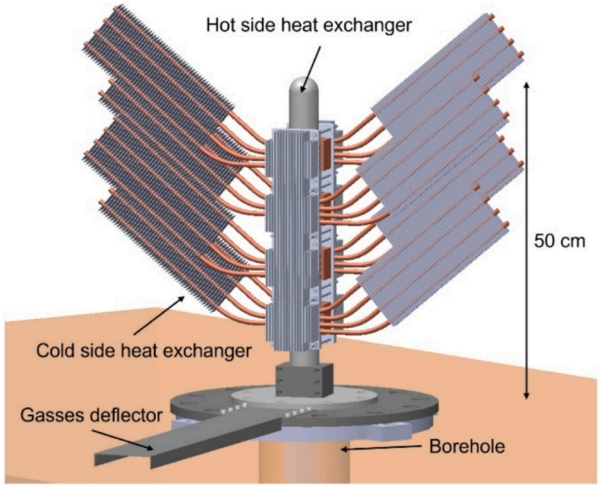

Fig. 1. Schematic illustration of a Geothermal TEG system developed by [27].

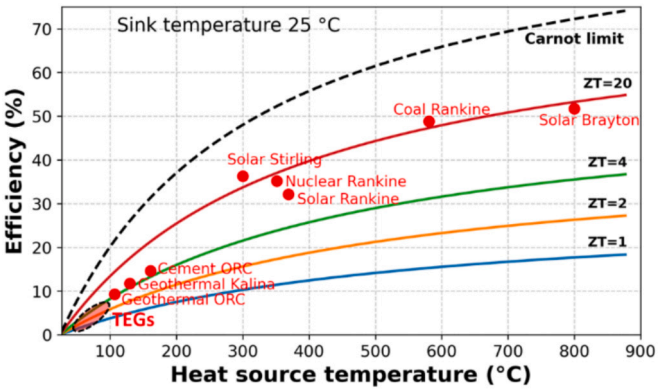

Fig. 2. TEG efficiency comparison with some best practice mechanical heat engines [32].

Conventional TEGs are based on bulk materials with limited shape conformability (typically planar TE modules) and require complex, expensive manufacturing processes. Thus, this technology seems to be costlier than other energy conversion methods, i.e., conventional geothermal plants, as TEG modules are one of the most expensive parts in the system [28]. However, the use of printing technologies for TEGs (screen printing and 3D printing) offers a potential solution to these challenges of shape conformability and cost-intensive manufacturing [33–35]. The main advantage of printing technologies lies in their automatability and scalability in the manufacturing processes (see Fig. 3).

We recently conducted a theoretical study on integrating printed TEGs into plate heat exchangers within 5th generation district heating (5GDH) systems, integrating geothermal, process waste heat, or solar thermal energy storage systems [36]. Printed TEGs could improve the cost-effectiveness of TEGs for geothermal energy applications.

Although several studies [13,15,23–28] on geothermal TEGs (GTEGs) using commercially available flat thermoelectric modules have previously been conducted by some of the co-authors of this work; this approach offers substantial scope for further investigation and improvement, particularly with respect to material selection and TEG device architecture. In the present study, we address a key aspect of GTEG development by systematically examining devices based on printed and bulk thermoelectric materials, including their shape-adapted design and fabrication. Specifically, we design, optimize, and evaluate the potential performance of printed geothermal TEGs (p-GTEGs) and bulk geothermal TEGs (b-GTEGs) under the geothermal application scenario described in [15]. We further estimate the TEG and system-level costs required to generate one unit of electrical power (€/W) and assess the levelized cost of electricity (LCOE, €/kWh) for both configurations. The influence of electrical and thermal contact resistances at the thermoelectric leg–conductor and TEG–thermosyphon/heat-sink interfaces on overall device behavior is also analyzed. Overall, this work provides the first systematic performance and cost comparison between printed and bulk TEG technologies for geothermal applications.

2. System design and components

Our research is inspired by the thermosyphon approach toward generating electricity from geothermal anomalies using TEGs [15]. In the original approach [15], planar bulk TEGs are integrated with a thermosyphon designed to capture geothermal energy from an anomaly located at Casa de los Camelleros. The temperature of hot gases emerging from a borehole and interacting with the lower part of the thermosyphon is ~170 °C (c.f. Fig. 4). In this work, we evaluate the potential integration of *printed* TEGs in two configurations, a) radial and b) planar, as shown in Fig. 4, into the same thermosyphon. In the radial

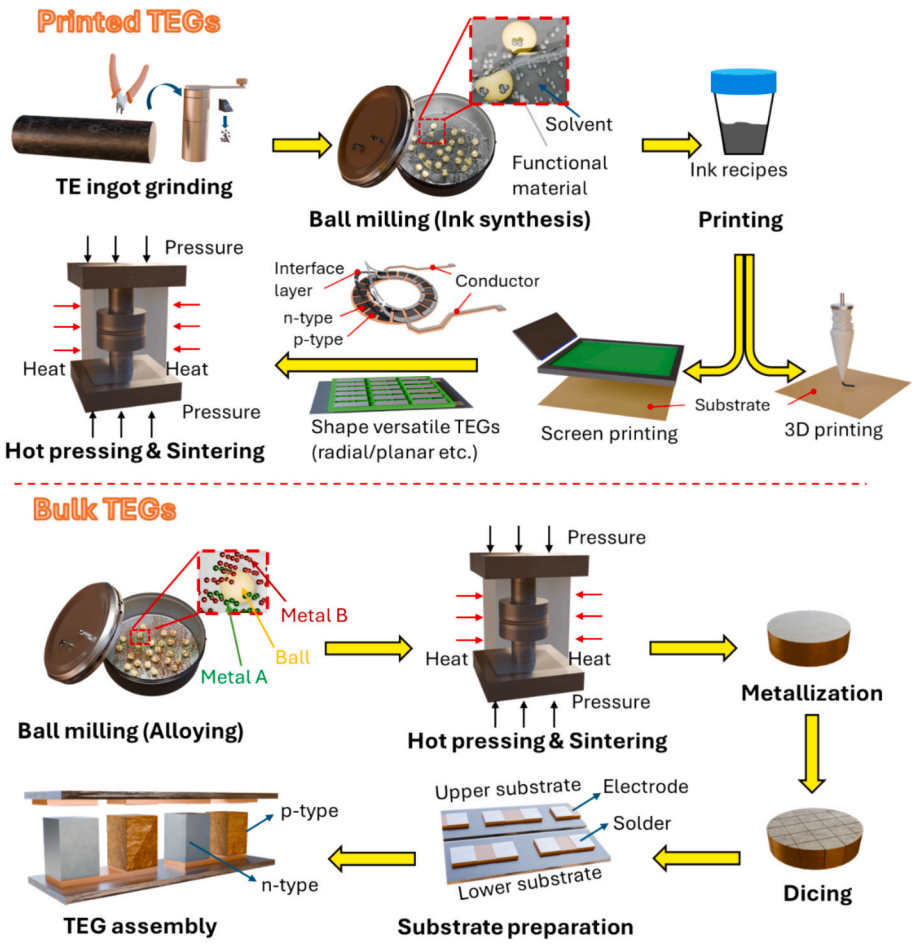

Fig. 3. Fabrication flow chart printed and bulk TEGs. Some visual elements were created in Blender using Blender Kit assets.

configuration, the alternating n- and p-type legs point outward from the cylindrical pipe and form a ring, which can be stacked in the z-direction. In the device, the substrates are aligned vertically with the pipe axis, whereas in the planar TEG, the mechanically flexible device is wrapped around the thermosyphon.

2.1. Thermosyphon

The use of efficient heat exchangers on both sides of the TEGs is just as crucial as employing materials with a high figure of merit (ZT) in the device [37]. Astrain et al. [38] effectively demonstrated that a reduction of 10% in the thermal resistance of the heat exchangers results in an 8% improvement in power generated by the TEGs. In this work, a large copper two-phase thermosyphon is selected as the hot-side heat exchanger, characterized by the geometrical specifications listed in Table 1.

The lower part of the thermosyphon is considered water-filled up to a specified limit of 375 mm. Rectangular aluminum fins are used to improve convection heat transfer between the hot gases from dry rocks and the thermosyphon. As hot gases (~170 °C) flow along the fins and the thermosyphon, the inside water absorbs the heat and starts to vaporize. Driven by density differences, the vapor is transported to the upper section, where it condenses and releases its latent heat of condensation to the TEGs. Before reaching the hot side of the TEG part, the heat transfer path includes several individual thermal resistances—namely, convection resistance Ψ^H_{conv}, conduction resistance $\Psi^H_{k_1}$, boiling resistance Ψ^H_{boi}, condensation resistance Ψ^H_{con}, and conduction resistance $\Psi^H_{k_2}$ in the condensation zone. The convection resistance Ψ^H_{conv} can be calculated analytically by using the following Eq. (1).

$$\Psi^H_{conv} = \frac{1}{h^H_{conv} \cdot A^H_{conv} \cdot \eta^H_f} \tag{1}$$

Here, h^H_{conv} represents the convection heat transfer coefficient taken as 20 W/(m^2·K) at the interface between the hot gases and the thermosyphon. A^H_{conv} is the area of the thermosyphon in contact with the hot gases (considering the fins as well as the area of the thermosyphon up to the water level). Fins improve convection heat transfer from the hot gases to the thermosyphon surface by reducing thermal resistance Ψ^H_{conv}. Their efficiency is calculated by following Eq. (2) [39].

$$\eta^H_f = 1 - \frac{n_f \cdot A_f}{A^H_{conv}} \left(1 - \frac{\tanh\left(m_f \cdot l_{chf}\right)}{m_f \cdot l_{chf}}\right) \tag{2}$$

where, n_f and A_f are the number of fins and the area of one fin, respectively. m_f is the thermal fin parameter determined by $m_f = \sqrt{\frac{2 \cdot h^H_{conv}}{\kappa_f \cdot t_f}}$ and $l_{chf} = l_f + \frac{t_f}{2}$ is the characteristic length of the fin.

A simple thermal circuit of the hot side heat exchanger, TEG part, and cold side heat exchanger is shown in Fig. 5.

Except Ψ^H_{conv}, all other thermal resistances before the hot side of the TEGs are taken as an internal thermal resistance of the thermosyphon $\Psi^H_{int} = \left(\Psi^H_{k_1} + \Psi^H_{boi} + \Psi^H_{con} + \Psi^H_{k_2}\right) = 0.11\ K/W$, as determined empirically by Alegria et al. [27].

2.2. Thermoelectric generator

The part of the thermosyphon above ground features TEGs mounted

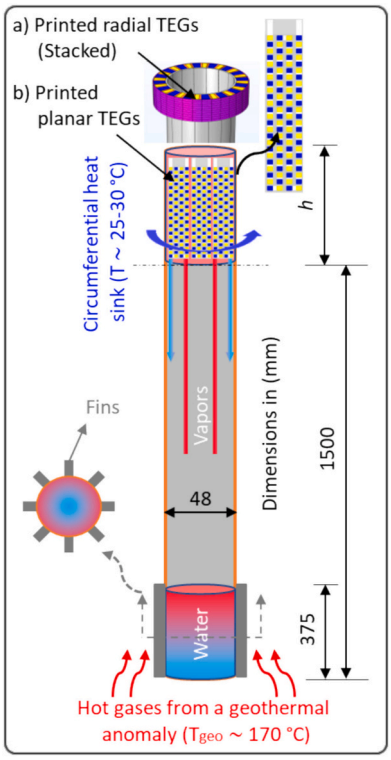

Fig. 4. Schematic thermosyphon integrated with the printed TEGs.

Table 1
Geometrical parameters of the two-phase thermosyphon used in the model [15].

Parameters	Value
Diameter, d (mm)	48
Thickness, t (mm)	1.5
Depth (below ground), y (mm)	1500
Height (above ground), h (mm)	Variable (100, 200, 500-mm)
Water level, w (mm)	375
No. of fins attached, n_f	31
Fin length, l_f (mm)	17
Fin thickness, t_f (mm)	2

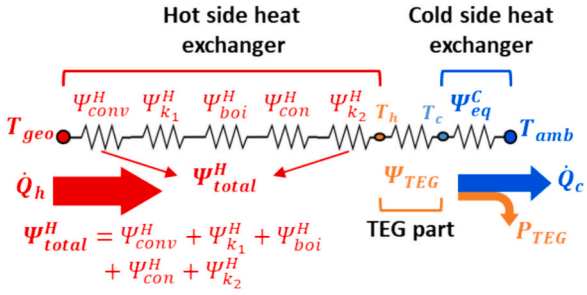

Fig. 5. Thermal circuit of the setup.

directly onto its outer surface. The vapors in the internal volume of the thermosyphon condense and transfer their latent heat of condensation to the TEGs, raising the temperature to T_h. In this way, conduction heat transfer occurs from the hot side of the TEGs to the cold side, having a temperature T_c. As long as a temperature gradient exists across the TEGs, they convert some of the heat flow $\dot{Q}_h$ from the hot reservoir into electrical power P_{TEG}, while the remaining heat flow $\dot{Q}_c$ is delivered to the heat sink (see Fig. 6) [40]. The energy balance at the nodes gives the electrical power output from the TEGs as presented in the following

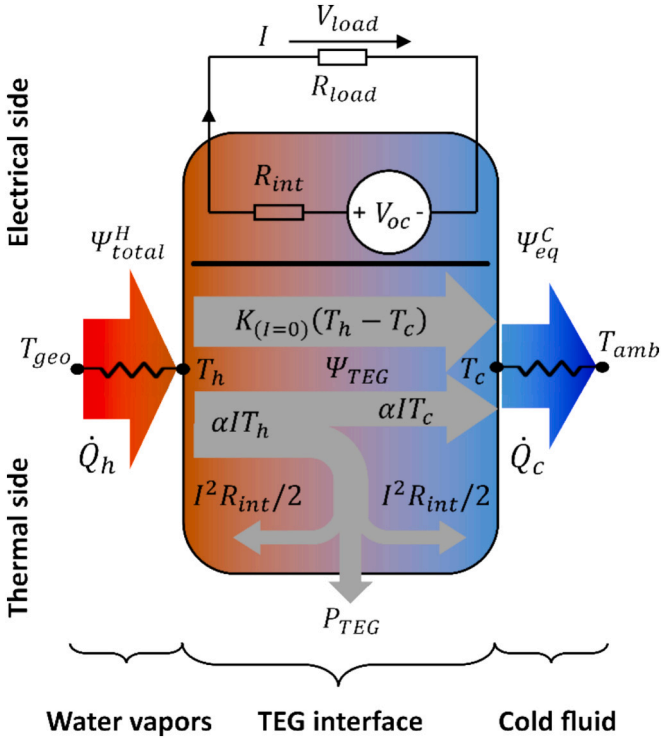

Fig. 6. Mathematical thermoelectrical picture of the TEG.

equations Eqs. (3)–(5).

$$\dot{Q}_h = \frac{T_{geo} - T_h}{\Psi^H_{total}} = \alpha \cdot I \cdot T_h - \left(I^2 \cdot R_{int}\right) \Big/ 2 + K_{(I=0)} \cdot (T_h - T_c) \tag{3}$$

$$\dot{Q}_c = \frac{T_c - T_{amb}}{\Psi^C_{eq}} = \alpha \cdot I \cdot T_c + \left(I^2 \cdot R_{int}\right) \Big/ 2 + K_{(I=0)} \cdot (T_h - T_c) \tag{4}$$

$$P_{TEG} = \dot{Q}_h - \dot{Q}_c = \alpha \cdot I \cdot (T_h - T_c) - I^2 \cdot R_{int} \tag{5}$$

2.2.1. TEG design consideration

There are two proposed design layouts to be integrated directly to the exterior part of thermosyphon: (a) radial layout and (b) planar layout (see Fig. 4). The radial layout involves printing thermoelectric materials and interconnects on an electrically and thermally insulated substrate (e.g., polymer foil), then stacking multiple devices on top of each other to form a tubular system. In a planar layout, the materials are printed on an electrically insulating and thermally conductive substrate (e.g., passivated metal foil), then mounting thin and flexible strip-like devices next to each other on the thermosyphon. In both these architectures, thin substrates are desirable as long as mechanical robustness is not compromised. Use of a thin substrate in radial designs minimizes parasitic in-plane heat flow. In contrast, in planar designs, it reduces thermal resistance and promotes efficient heat flow to the device, thereby improving overall TEG performance in both cases. In printed thermoelectrics, device thickness is generally limited by the manufacturing process (considering screen printing). In our work, we assume a maximum device thickness of $t_{TEG} \sim 1$ mm for screen-printed devices, while thicker devices ($t_{TEG} > 1$ mm) can be achieved via 3D printing. The following section outlines the optimization criteria, explaining when and why a particular layout is considered suitable and, consequently, selected.

2.2.2. Optimization criteria and design selection

Although there are two different configurations of the TEGs, the underlying optimization principles applied to both configurations

remain the same. The general criteria for simultaneous thermal and electrical impedance optimizations must be fulfilled to ensure the TEG system delivers maximum electrical power output. These optimum conditions are met only when the TEG's electrical resistance R_{int} match load electrical resistance R_{load}. In contrast, due to the coupled thermal–electrical behavior of TEGs as well as different fill factor designs, the effective internal thermal resistance of TEG Ψ_{TEG} needs to be tuned to achieve an optimal ΔT_{TEG} and maximize power density in operation mode (detailed discussion in Sections 4.1 and 4.2).

The fill factor F (ratio of active TE area to the total device area) and the leg dimension (length l_{TEG} in radial design and thickness t_{TEG} in planar design) of a TEG device are two interdependent, crucial parameters to achieve these two optimization criteria simultaneously. At a specific fill factor, a unique leg dimension optimizes the device for maximum power output. This leg dimension is also strongly influenced by the heat transfer coefficients at the heat source and sink interfaces. When these heat transfer coefficients are high enough to achieve impedance matching at shorter leg dimensions (<1 mm), a planar device similar to conventional TEGs is better suited due to its ease of handling and integration into the system. Lower heat transfer coefficients result in a higher optimal leg dimension (>1 mm). In that case, fabricating a planar TEG becomes challenging due to limitations in the manufacturing process (screen printing). In such cases, radial layout becomes a viable alternative, although it is more difficult to handle mechanically and to scale up through stacking. Nevertheless, in terms of the fill factor degree of freedom, the radial design offers a larger parameter range than the planar one. This is because the maximum achievable fill factor in planar layouts, considering printability constraints, is approximately ~0.5–0.6, whereas in radial layouts it can reach ~0.7–0.8, enabling higher power density under similar boundary conditions.

2.3. Heat sink

In thermoelectric power generation, an efficient heat sink is essential to achieve optimal performance. Several studies have examined heat sinks and their performance in enhancing thermoelectric power generation [41–44]. Elghool et al. [45,46] conducted studies on different types of heat sinks and their optimization for TE power generation, and concluded that passive heat-pipe-based heat sinks are most suitable for the medium-temperature range (<300 °C). In another study on the same heat pipe-based heat sinks, they performed multi-objective optimization under forced convection to evaluate the optimal heat sink geometry, maximizing TEG power output and efficiency while minimizing cost [47]. They also evaluated TE performance with two different heat pipe materials (one made of copper and the other of aluminum) and found copper-based heat pipes to be more efficient than aluminum-based heat pipes [48]. In this work, we assumed copper-based heat pipes to dissipate heat from the cold side of the TEGs. For the COMSOL simulations, an effective convection heat transfer coefficient h_{eff} of 5000 W/(m^2·K) is considered for the heat pipes. The value of the effective heat transfer coefficient h_{eff} was estimated from the following empirical thermal resistance equation derived by Alegria et al. [15] based on an average wind velocity V_w of 20–30 km/h. The corresponding equivalent thermal resistance ranged from 0.1312 to 0.1150 K/W per TEG module (40 × 40 mm). So, the $h_{eff} = 1/\left(\Psi^C_{eq}\cdot A_{module}\right)$ values fall within the range of approximately 4762 to 5435 W/(m^2·K).

$$\Psi^C_{eq} = 0.3485\cdot\left(\frac{V_w}{\frac{km}{h}}\right)^{-0.326} K\Big/W \tag{6}$$

3. Modeling and simulation

COMSOL Multiphysics 6.2 is employed for modeling and simulation due to its robust capability to handle complex, coupled multi-physics phenomena, such as thermoelectrics. Note, for simplicity and computational efficiency, only 1/16 part of the system was simulated for three different TEG heights (h = 100, 200, and 500 mm, c.f. Fig. 7). We have considered a cylindrical sector of the thermosyphon and modeled one radial thermocouple to optimize its parameters for maximal output power. Respective material properties were assigned to all components of the modeled thermocouple. A thin Kapton sheet was used as the substrate, while n-type Bi_2Te_3-based and p-type Bi_2Te_3-based compounds served as the TE materials [49]. Carbon paste was introduced as a diffusion barrier between the electrodes and the TE materials. Copper was designated as the electrode material, and glass (with low κ_{fill} ~ 0.1 W/(m·K)) was employed both as a dielectric and as a filler to provide structural support, particularly when the screen-printed thickness is increased or when the device is 3D printed to achieve even more thickness. However, for simulating bulk TEGs, no filler material is considered in the model for structural support, and resulting air gaps are considered with thermal conductivity of (κ_{air} ~ 0.028 W/(m·K)). In heat transfer boundary conditions, from the heat source to the hot side of the thermocouple, an analytical model based on Eqs. (1) and (2) and the modified empirical value of Ψ^H_{int} for the respective section (1/16 part) is fed into the COMSOL environment. On the cold side of the thermocouple, a convection boundary condition is applied with an effective convection heat transfer coefficient h_{eff} of 5000 W/(m^2·K) [15]. Under these two heat flux boundary conditions, the geometry of the modeled thermocouple is optimized with respect to an objective function (maximum power density $p_{d_{max}}$). In the *electric current* interface, one terminal is set to ground and the other to floating potential. In COMSOL Multiphysics, both the *thermoelectric effect* and *electromagnetic heating* were enabled for the relevant domains and at the corresponding boundaries. We employed a structured mesh with *extra fine* element size to ensure the accuracy of the simulations. To adequately handle the complexity of this multi-physics problem, a fully coupled solver was used in these simulations.

3.1. Multiparameter optimization

As previously discussed, fill factor and leg dimension are two important parameters that can be adjusted to optimize power output from the thermocouples and TEG devices. In this study, a '*Parametric Sweep*' is performed for these two variables, with leg dimension ranging

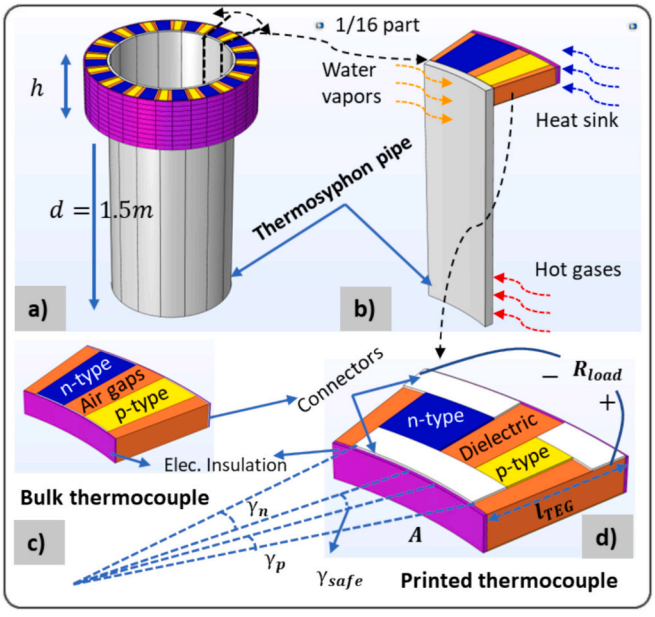

Fig. 7. (a) Thermosyphon illustration, (b) 1/16th part with one thermocouple, (c) bulk thermocouple, (d) printed thermocouple.

from 0.5 mm to a value at which simultaneous thermal and electrical impedance optimizations are achieved at the highest fill factor ($F \sim 0.9$) and fill factor F ranging from 0.1 to 0.9.

For each combination, the simulation goes to an optimization of the angle factor F_{ang} of the n-type and p-type legs, conductor width overlapping with TE materials (in printed TEGs only W_{cond}) as well as the electrical load resistance R_{load} between the ground and floating terminals (c.f. Fig. 8). Due to the mismatch in material properties between the n-type and p-type TE legs, the optimization solver determines an F_{ang} different from 0.5, resulting in different sector angles for each leg, as shown in Eqs. (7) and (8).

$$\gamma_n = \left(\frac{360}{n_{tc}} - 2{\cdot}\gamma_{safe}\right){\cdot}F_{ang} \tag{7}$$

$$\gamma_p = \left(\frac{360}{n_{tc}} - 2{\cdot}\gamma_{safe}\right){\cdot}(1 - F_{ang}) \tag{8}$$

Ultimately, the maximum power density (in W/m^2) obtained from the modeled thermocouple is recorded and visualized as a function of these two variables using contour plots (c.f. Fig. 9 and Fig. 10).

4. Results and discussion

As stated earlier, the design of TEGs to produce maximum power in any application scenario depends on simultaneous thermal and electrical impedance optimization. Regarding thermal impedance optimization, determining heat transfer coefficients in units of W/(m^2·K) or thermal resistances in units of m^2·K/W of heat source and heat sink (Ψ^H_{total} and Ψ^C_{eq}) – whether through simulation or experimental measurement is important. Once the thermal resistances on both sides of the TEGs are estimated, the heat flow through the device can be tuned by adjusting either the fill factor, leg dimension, or a combination of both, enabling the system to achieve an optimal temperature difference ΔT_{TEG} for maximum TEG power density. In our current application scenario, we determine normalized contact thermal resistances (in cm^2·K/W) of the thermosyphon for each of the three cases (h = 100, 200, and 500 mm; c.f. Fig. 7), and these normalized contact thermal resistances Ψ_{cont} per thermocouple differ across the three cases (see Table 2 and Table 3). In operation mode, a TEG delivers maximum power density at a specific internal thermal resistance Ψ_{TEG}, which depends on contact thermal resistances, material properties, device geometry and layout, as well as the electrical operating point through Joule and Peltier effects. Regarding electrical impedance matching, maximum power extraction from a voltage source is achieved when the load resistance (R_{load}) matches the source's internal resistance (R_{int}). The internal electrical resistances (R_{int}) of these devices are calculated in COMSOL at given conditions by simultaneously measuring the current and the voltage across the terminals, accounting for the respective material properties and device geometry. The materials parameter for the bulk case is used as given in the COMSOL database; the parameters for the printed materials were determined in our own experimental study [49]. Therefore, both thermal and electrical impedance conditions must be satisfied in the design of TEGs.

4.1. Performance and cost estimation of printed TEGs

Once the boundary conditions, such as heat transfer coefficients or thermal resistances of the heat source and heat sink, are defined, printed TEGs offer greater design flexibility to optimize power output without requiring modifications to the source or sink. Fig. 9(a–c) illustrates the contour maps of power density for printed TEGs for three different heights. Among the three scenarios, the highest power density is achieved for a TEG height of 100 mm. As the height increases to 200 mm and 500 mm, the power density gradually decreases. This decrease in power density is primarily due to a reduction in heat flow per mm of height (h). However, the overall heat flow from the heat source to the hot side of the TEGs–and ultimately to the heat sink increases due to a parallel thermal resistance network, leading to a low value of equivalent total thermal resistance. To maintain optimal performance and achieve maximum power density under these conditions, it is necessary to increase the leg dimensions to achieve the thermal impedance condition. It can be seen that, at the maximum fill factor (case I), printed TEGs exhibit somewhat higher performance than bulk TEGs across all three scenarios (h = 100, 200, and 500 mm). However, as the fill factor decreases (Case II), the optimal power density drops more rapidly in printed TEGs compared to bulk TEGs. This drop is due to parasitic heat losses through the substrate area and filler material (~0.1 W/(m·K)). In contrast, bulk TEGs exhibit lower parasitic heat flow through air gaps (~0.028 W/(m·K)), because no substrate is considered, thereby minimizing these losses. Table 2 shows the normalized thermal resistances of contacts and TEGs for different scenarios. For the first two scenarios (h = 100 & 200 mm), TEGs with ~0.9 fill factors show almost similar contact and TEG thermal resistances ($\Psi_{TEG} \cong \Psi_{cont}$) for maximum power density output. However, lower fill factor ~0.3 TEGs show thermally over-matched impedance ($\Psi_{TEG} > \Psi_{cont}$) for maximum power density, where they acquire a ΔT_{TEG} of around 96 °C and 90 °C (see Fig. 9d and e, respectively) at optimized geometries. The TEGs for the 3rd scenario (h = 500 mm) show thermally under-matched impedance ($\Psi_{TEG} < \Psi_{cont}$) to achieve maximum power density. The reason is the complex interplay of current flow, increasing electrical resistance, and the Joule and Peltier effect, which is why increasing the internal thermal resistance of TEG Ψ_{TEG} further to approach Ψ_{cont} results in more loss than gain.

In Fig. 9, Case I and Case II represent simultaneous thermal and electrical impedances tuned to achieve maximum power density for devices with fill factors of ~0.9 and ~0.3, respectively. Case III, on the other hand, corresponds to an electrically impedance-matched but thermally under-matched device, with a 1 mm leg dimension, feasible for screen printing to produce a flexible planar device structure rather than a radial one. Although printed TEGs exhibit lower performance at reduced fill factors than bulk TEGs, they require significantly less thermoelectric material per watt, thereby reducing costs (€/W). Additionally, the fabrication cost of printed TEGs is substantially lower than that of bulk TEGs. This highlights an important cost-performance trade-off in opting for thermoelectric devices (printed or bulk). Fig. 9 (d–f) and (g–i)

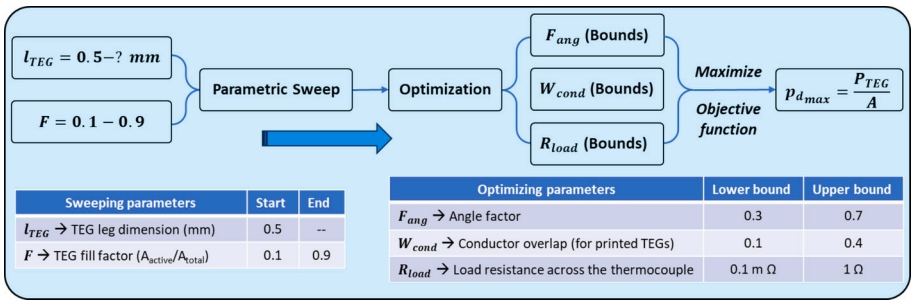

Fig. 8. Block diagram of the COMSOL Multiphysics parametric sweep and optimization process.

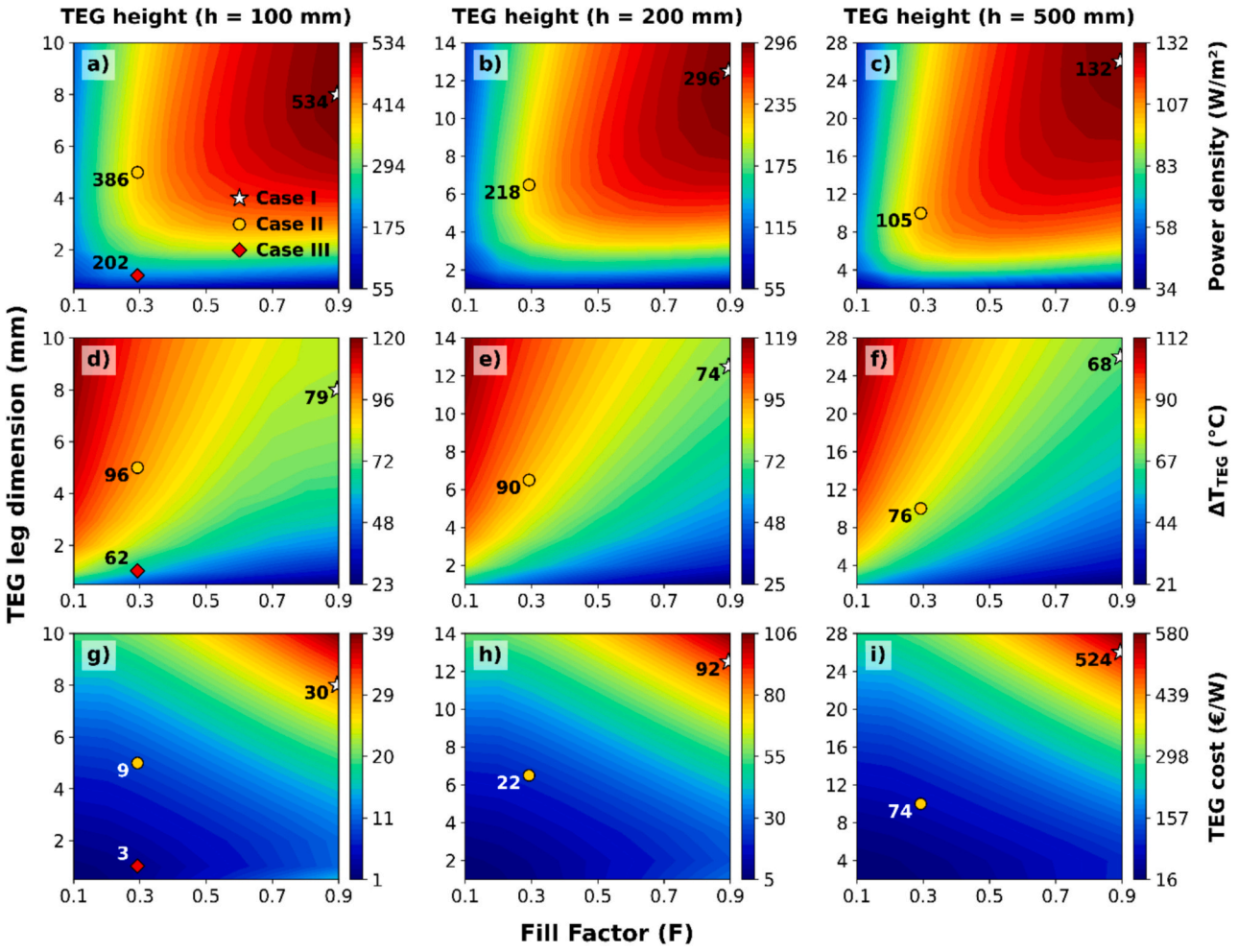

Fig. 9. Printed TEG optimization for different heights 'h', (a–c) Power density contours (W/m^2), (d–f) ΔT_{TEG} across TEG sides (°C), (g–i) TEG costs per watt (€/W). Case I refers to a fill factor of $F \sim 0.9$, while case II represents a fill factor of $F \sim 0.3$. Case III stands for a printed planar TEG (see text) with a fill factor of $F \sim 0.3$.

illustrate the optimal temperature difference ΔT_{TEG} to be maintained and the TEG cost per watt (€/W), respectively. Fig. 9 (g–i) illustrates the costs (€/W) associated with TEGs only required to generate one watt of electrical power (see Supplementary Information for details of the cost model). However, the total system cost (TEG cost + Thermosyphon system cost) estimation is projected in Section 4.4.

4.2. Performance and cost estimation of bulk TEGs

Conventional bulk TEGs are generally available in flat, planar modules. In this study, we simulated bulk TEGs adapted to our specific application geometry (thermosyphon) to evaluate and compare their performance with that of our in-house-printed TEGs of the same configuration. In Fig. 10(a–c), we present simulated results of bulk TEGs under the same boundary conditions as described above. For each scenario, a specific region is observed at a particular fill factor and leg dimension combination, where the maximum power density is achieved for both printed and bulk devices. Any offset from this optimal combination results in a reduction in power density. It can be observed that, for bulk radial TEGs, a combination of high fill factor and high leg dimensions is not necessarily a good choice, as comparable performance can be achieved with a lower fill factor and smaller leg dimensions, significantly reducing the TE material required. In Fig. 10(d–f), we illustrate the temperature difference ΔT_{TEG} across TEG sides to be maintained to get maximum power output from the designed TEGs. Deviating from this optimal condition, either by increasing the thermal resistance of the device through a lower fill factor or larger leg dimensions, or by reducing it via a higher fill factor or smaller leg dimensions, leads to a reduction in power density. The former approach can yield higher ΔT_{TEG}; however, it leads to reduced power density due to decreased active material when the fill factor is lowered and increased electrical resistance when the leg dimension is increased, which offsets the benefits of the higher ΔT_{TEG}. The latter approach reduces the temperature difference across the device by increasing the fill factor or decreasing the leg dimensions, thereby lowering the power density. If both parameters are adjusted so that the device satisfies both thermal and electrical impedance optimizations, comparable power density can be achieved more economically (at lower fill factor and leg dimensions – see Case I and Case II). Table 3 shows the normalized thermal resistances of contacts and TEGs for different scenarios. For the first scenario (h = 100 mm), the TEGs show almost similar contact and TEG thermal resistances ($\Psi_{TEG} \cong \Psi_{cont}$) for maximum power density output. However, TEGs for the other two scenarios (h = 200 & 500 mm) show thermally under-matched impedance ($\Psi_{TEG} < \Psi_{cont}$) to achieve maximum power density due to the dominating Joule and Peltier effects, which suppress the benefits coming from higher ΔT_{TEG} by increasing internal TEG thermal resistance Ψ_{TEG} further to approach Ψ_{cont}.

Fig. 10(g–i) illustrates the costs (€/W) associated with TEGs only required to generate one watt of electrical power. As the fill factor and leg dimensions are reduced to meet the optimization criteria, material consumption decreases significantly with minimal compromise in power density. The contour plots show TEG costs per watt (€/W) at varying

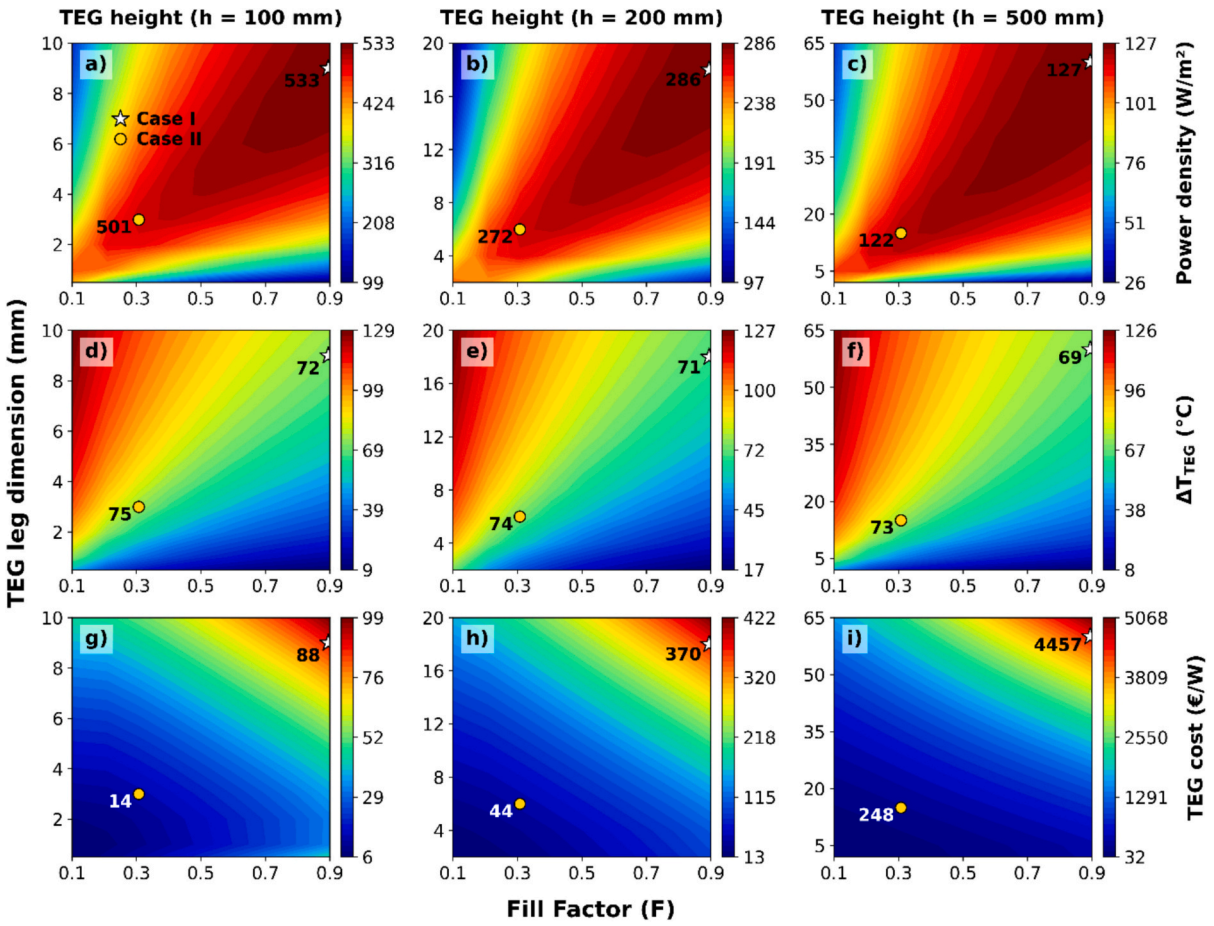

Fig. 10. Bulk TEG optimization for different heights 'h', (a–c) Power density contours (W/m^2), (d–f) ΔT_{TEG} across TEG sides (°C), (g–i) TEG costs per watt (€/W). Case I refers to a fill factor of ~0.9, while case II represents a fill factor of ~0.3.

Table 2
Normalized thermal resistances for different scenarios (printed TEGs).

TEG heights	Fill factor	Leg dimension l_{TEG} (mm)	Normalized contact resistances Ψ_{cont} (cm^2·K/W)	TEG thermal resistance Ψ_{TEG} (cm^2·K/W)
h = 100 mm	~0.3	5	39.4	76.7
	~0.9	8		40.4
h = 200 mm	~0.3	6.5	77.8	89.5
	~0.9	12.5		77.7
h = 500 mm	~0.3	10	191.5	168.5
	~0.9	26		165.8

Table 3
Normalized thermal resistances for different scenarios (bulk TEGs).

TEG heights	Fill factor	Leg dimension l_{TEG} (mm)	Normalized contact resistances Ψ_{cont} (cm^2·K/W)	TEG thermal resistance Ψ_{TEG} (cm^2·K/W)
h = 100 mm	~0.3	3	39.4	39.3
	~0.9	9		38.9
h = 200 mm	~0.3	6	77.8	75.6
	~0.9	18		70.1
h = 500 mm	~0.3	15	191.5	172.2
	~0.9	60		163.5

TEG heights, fill factors, and leg dimensions, providing insight into cost-efficiency trade-offs. It is important to note that as the TEG height increases (100 mm–500 mm), optimal performance for both printed and bulk TEGs tend to occur at larger leg dimensions for a given fill factor. However, this is not an economically favorable solution due to increased material usage.

The detailed costs for TEGs for a fill factor of ~0.3, including components and fabrication, are shown in Fig. 11. Further details of the cost for each step in the printing and bulk approaches are provided in the Supplementary Information. At a TEG fill factor of ~0.3, the printed and bulk approach radial TEG costs are presented in Fig. 11, which indicates that printed TEGs are a more cost-effective choice. For a planar printed TEG case, the price is even lower than this (see Fig. 9, Case III).

4.3. *V–I and P_d–I performance comparison: printed vs bulk TEGs*

We now compare the V–I and P_d–I performance characteristics of printed and bulk TEGs. Two radial devices, one printed and one bulk, are simulated at two different fill factors of ~0.3 and ~0.9. Their respective characteristic curves are presented in Fig. 12(a–b) for comparison. For clarity and ease of comparison, the same scales are used on both the x and y axes when plotting the characteristics of printed and bulk TEGs. As expected for a device dominated by Ohmic behavior, a linear relationship between output voltage and current is observed across all devices. The maximum power density is almost the same for the two device types, at approximately 0.5 kW/m^2 for a fill factor of ~0.9. For a lower fill factor of ~0.3, however, the drop in TEG power density in printed TEGs is substantially more pronounced than in bulk TEGs. This can be explained by the more critical role of parasitic heat transfer in the case of a printed device.

Fig. 13 presents the COMSOL 3D simulation results showing temperature and electric potential distributions of printed TEGs at two different fill factors: ~0.3 (top row) and ~0.9 (bottom row).

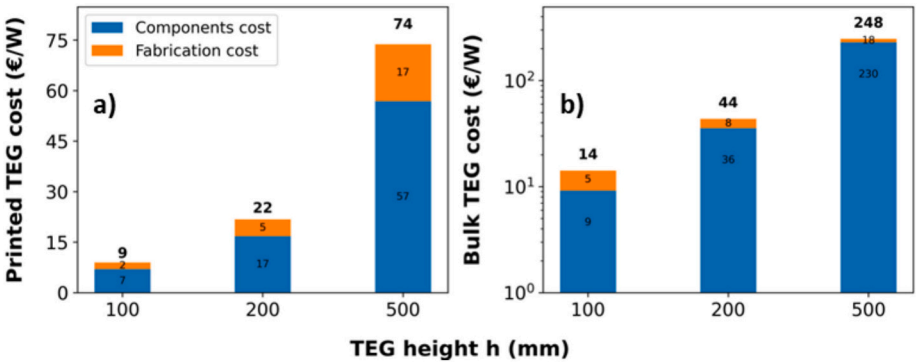

Fig. 11. TEG components and fabrication costs per watt (€/W), (a) printed TEGs, (b) bulk TEGs.

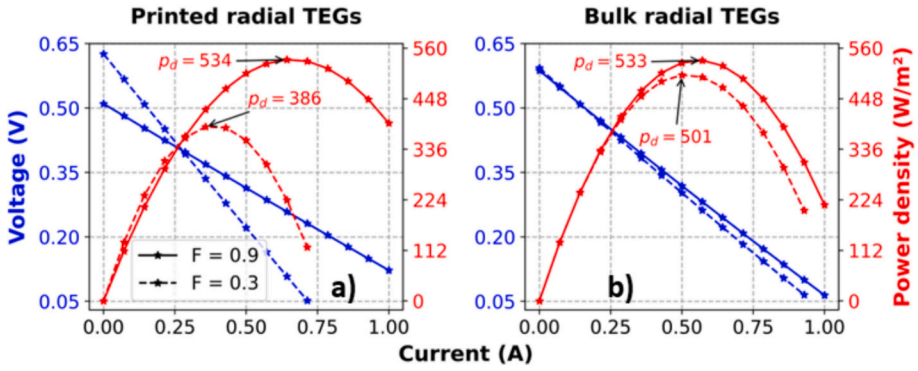

Fig. 12. V–I and P_d–I characteristics curves, (a) printed radial TEGs, (b) bulk radial TEGs.

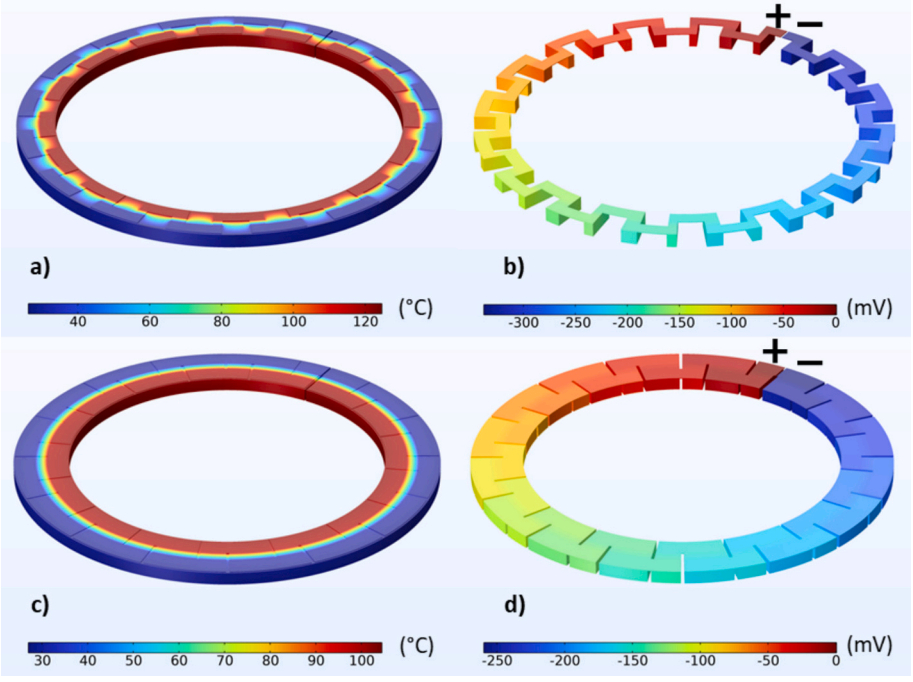

Fig. 13. COMSOL 3D plots for printed TEGs, (a) temperature at $F \sim 0.3$, (b) electric potential at $F \sim 0.3$, (c) temperature at $F \sim 0.9$, (d) electric potential at $F \sim 0.9$.

In the case of a low fill factor, the reduced thermal conductivity of the filler material, combined with the high thermal conductivity of the electrodes, results in significant deviations from purely circular symmetry in the temperature distribution.

Fig. 14 presents the COMSOL 3D simulation results for the temperature and electric potential distributions in bulk TEGs at two different fill factors: ~0.3 (top row) and ~0.9 (bottom row). As the electrodes are extended vertically, they do not alter the temperature distribution in bulk TEGs.

We also simulated a planar thermocouple configuration (Case III of

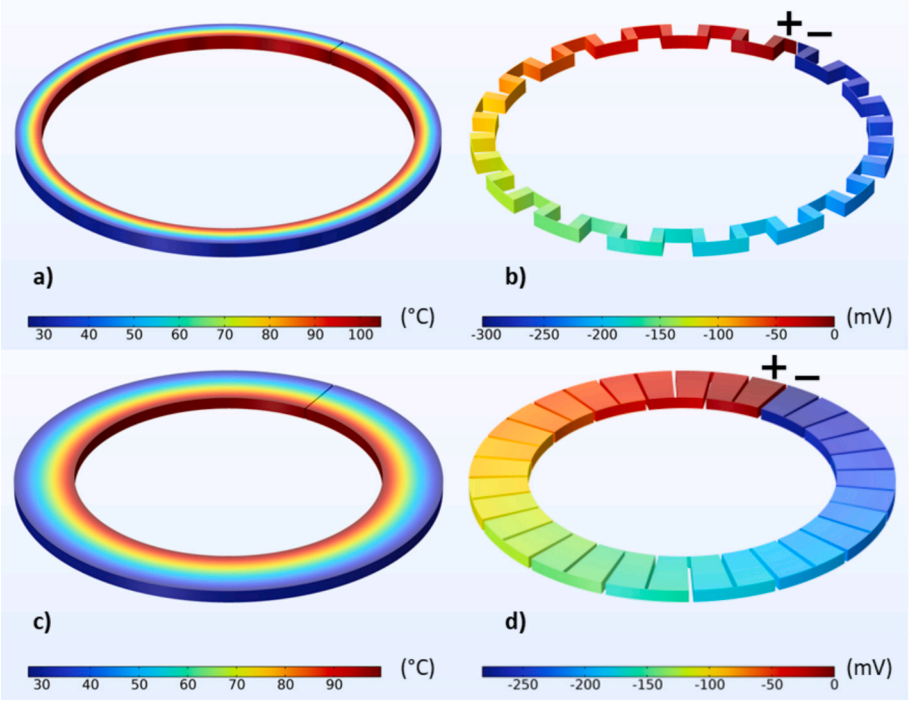

Fig. 14. COMSOL 3D plots for bulk TEGs, (a) temperature at $F \sim 0.3$, (b) electric potential at $F \sim 0.3$, (c) temperature at $F \sim 0.9$, (d) electric potential at $F \sim 0.9$.

the printed TEGs, see Fig. 15) with a TEG thickness of 1 mm, to enable the attachment of multiple strip-shaped TEG devices to the outer surface of the thermosyphon. This planar device may not be thermally impedance optimized due to its low thermal resistance, but it is easy to fabricate and integrate onto the thermosyphon's outer surface. Such a design can be beneficial from an economic point of view as this configuration allows for a ~ 67% reduction in the TEG cost per watt (€/W), with a ~ 48% compromise in power density–showing a cost-performance trade-off. At a fill factor of ~0.3 and a thickness of 1 mm, the device sustains an average temperature gradient of ~62 °C and delivers an output power density of ~0.2 kW/m^2 (c.f. Fig. 15).

4.4. Power and cost estimation per thermosyphon pipe for different TEG heights

In the previous sections, we focused only on power densities (W/m^2). Here, in Fig. 16(a–b), the power output per thermosyphon pipe is calculated for different TEG heights for both printed and bulk radial TEGs. The y-axis scales for both plots are kept identical to clearly highlight the difference in power output between the two types of devices. Here as well, printed radial TEGs show almost a little bit higher performance than bulk radial TEGs in terms of power output at higher fill factors of ~0.9. However, at lower fill factors, such as ~0.3, the power drop in printed TEGs is more significant than in their bulk counterparts, primarily due to parasitic heat losses, as discussed in Section 4.1. Fig. 16(c–d) illustrates the printed and bulk TEG costs per watt (€/W) for fill factors of ~0.9 and ~0.3. For all cases, it is presented that printed TEGs are cost-effective compared to their bulk counterparts. Moreover, the manufacturing processes for bulk TEGs are typically complex and labor-intensive, whereas printed TEGs can benefit from scalable, cost-effective fabrication methods (c.f. Fig. 3). Our cost estimates are based on the prices and manufacturing costs of lab-scale TEG materials (see Supplementary Information for details). However, industrial-scale costs for TEGs very likely will be *lower* than we project here. Fig. 16(e–f) illustrates the normalized cost per watt of electrical power (€/W) for the entire thermosyphon system, including all hot- and cold-side heat exchanger components.

Fig. 17 presents the levelized cost of electricity LCOE (€/kWh) for a system life period of 25 years. The detailed calculations are presented in the Supplementary Information. LCOE values are lower at lower fill factors in all cases for both approaches (printed and bulk TEGs) with the one exception for a lower fill factor at a TEG height of 100 mm. Where,

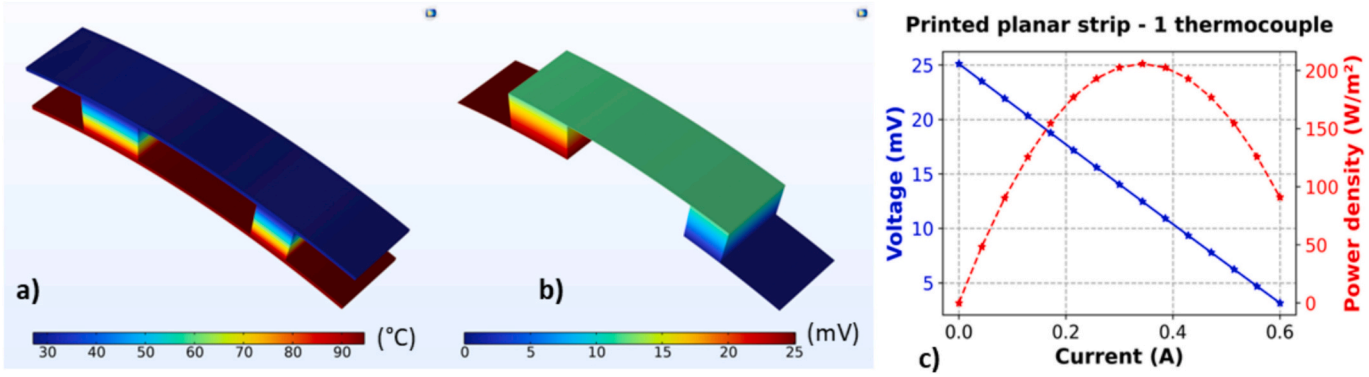

Fig. 15. COMSOL 3D plots for printed planar TEGs, (a) temperature at $F \sim 0.3$, (b) electric potential at $F \sim 0.3$, (c) V–I and P_d–I characteristics curves.

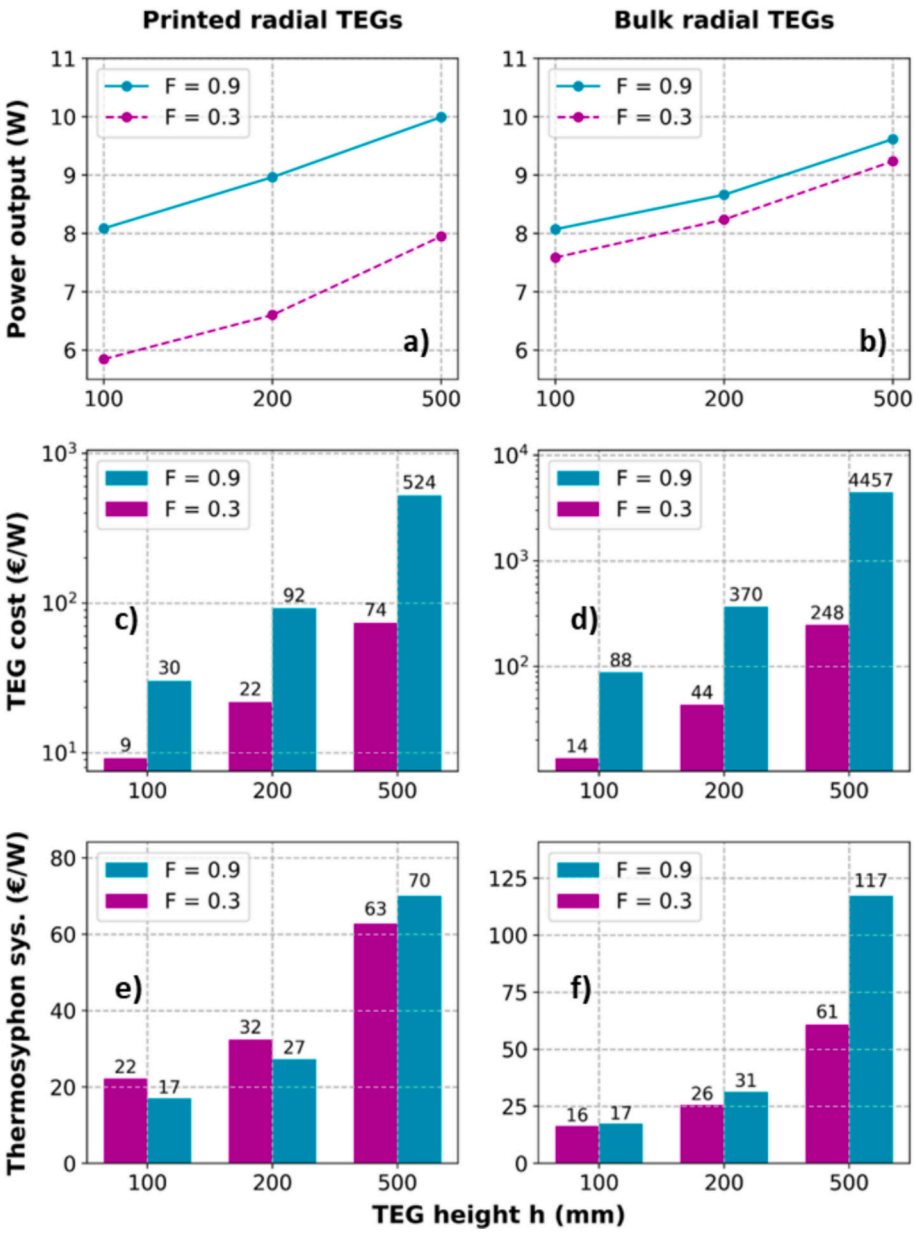

Fig. 16. Printed and bulk TEG comparison, (a–b) power output (W) (c–d) TEG cost (€/W), (e–f) thermosyphon system components cost (€/W).

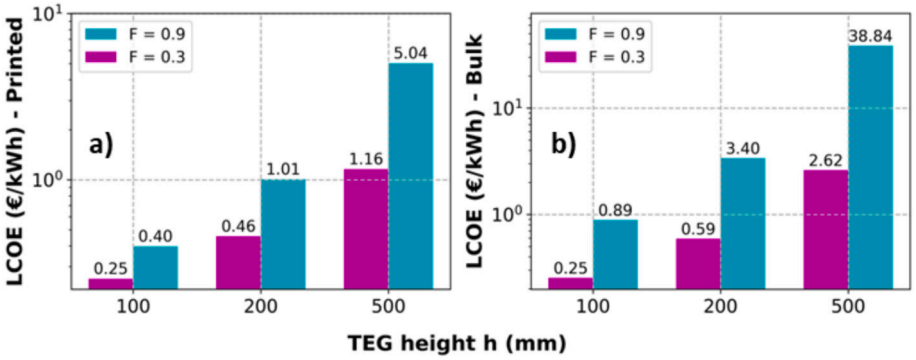

Fig. 17. Levelized cost of electricity (LCOE - €/kWh), (a) printed TEG system, (b) bulk TEG system.

due to low power at lower fill factors, the thermosyphon system cost (€/W) for printed TEGs case is slightly higher for lower fill factors and TEG heights of 100 mm (c.f. Fig. 16). As a result, at this fill factor and TEG height, the LCOE values of these two approaches are approximately

the same ~0.25 €/kWh.

Although this is an emerging technology still under research and development, the costs and power values are competitive for remote areas with geothermal anomalies that require a 24 h supply of electrical power from a few watts to several tens of watts, especially when climatic conditions do not favor the use of photovoltaics. Moreover, Geothermal ORCs are not suited for this micro-energy-harvesting application.

4.5. Effect of electrical and thermal contact resistances

Electrical and thermal contact resistances between TE legs and the conductor, and between the TEG and the thermosyphon/heat, may exist in reality. To analyze the effect of electrical contact resistances, we modeled a thermocouple with a geometry similar to the optimized design (h = 100 mm) for both printed and bulk devices. We inserted a so-called diffusion barrier/contact resistance domain between the TE material and the conductor. Fig. 18(a–b) shows the effect of different electrical resistivity values for this contact material, and the power density is plotted for both types of devices at two fill factors ($F \sim 0.3$ and ~0.9). As electrical resistivity increased, a drop in power density is observed. Hence, a good interface material is critical to maintaining performance. Fig. 18(c–d) shows the effect of thermal resistivity of a modeled thermal domain, which acts as an electrical insulator between the thermosyphon and TEG and the heat sink and TEG.

Regarding thermal contact resistances, we considered only two junctions that serve both as electrical insulators and contact materials. One on the hot side between the thermosyphon and the TEG, and the other between the TEG and the heat sink – shown in purple color in the thermocouple in Fig. 7 (thickness = 200 μm). We plotted the power density against various thermal resistivity values of these modeled domains, assuming carbon paste as a diffusion barrier (5 μm resulting in 40 S/cm). As thermal resistivity increases, power density also drops for both types of devices. So, it is always crucial to minimize these resistances (both electrical and thermal) to achieve good performance. The reduction in power density at higher resistances results in a corresponding increase in both the cost per watt and the LCOE values.

5. Conclusion

In this study, we have compared the performance optimization of thermosyphons equipped with TEGs for energy harvesting in the context of geothermal anomalies. We have compared printed thermoelectric devices with conventional thermoelectric devices based on bulk materials for geothermal energy harvesting. COMSOL simulations were conducted for three different TEG heights (h = 100, 200, and 500 mm), while keeping the thermal resistance of the bottom portion of the thermosyphon constant. For each situation, we have optimized the TEG design and compared different fill factors. The most favorable design depends on the user's requirements. The minimum LCOE is achieved at the smallest investigated TEG height of 100 mm for both printed- and bulk-TEG devices. This is explained by the higher power density and the resulting lower TEG cost per watt (€/W). We predict LCOE of ~0.25 €/kWh for both approaches, printed and bulk TEGs, respectively. The electrical power for this design amounts to ca. 6 W for the printed TEGs and 7.5 W for bulk TEGs. Higher power can be achieved for larger TEGs in both cases. This, however, results in higher LCOE. The costs and power values are competitive for remote areas with geothermal anomalies where a 24 h supply of electrical power is needed, especially when climatic conditions do not favor the use of photovoltaics.

CRediT authorship contribution statement

Muhammad Irfan Khan: Writing – original draft, Software, Methodology, Formal analysis, Conceptualization. **Leonard Franke:** Writing – review & editing, Conceptualization. **Andres Georg Rösch:** Writing – review & editing. **Zirui Wang:** Visualization. **Md. Mofasser Mallick:** Writing – review & editing, Data curation. **Patricia Alegría:** Writing – review & editing, Data curation. **Nerea Pascual:** Writing – review &

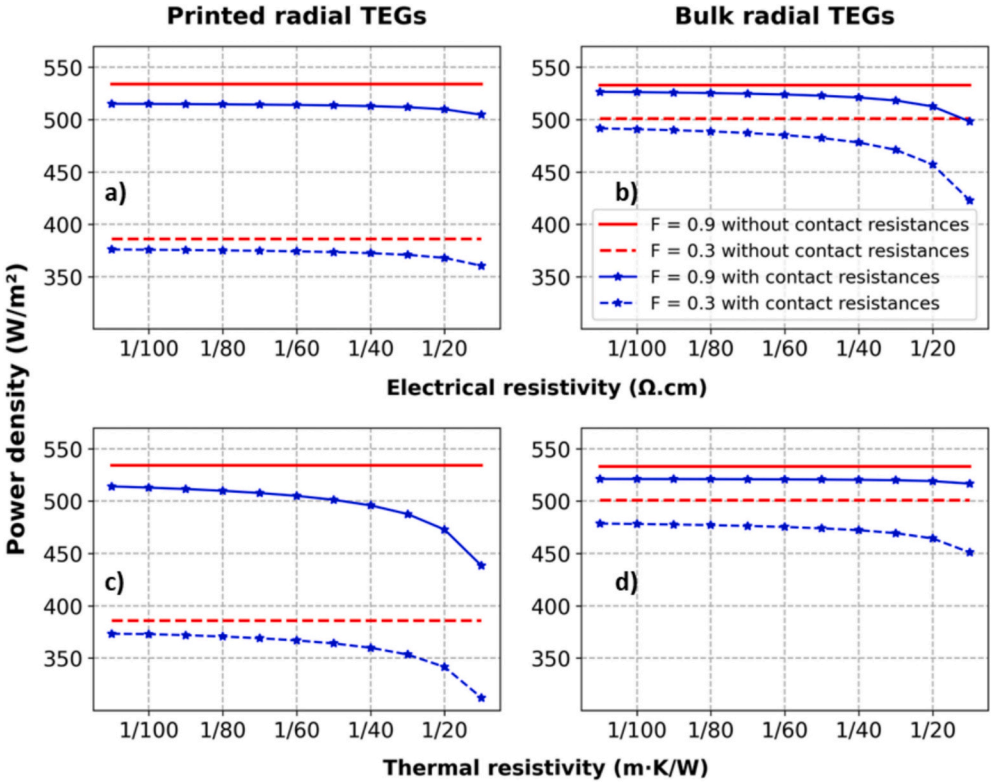

Fig. 18. Effect of contact resistances, (a) printed radial TEGs performance vs electrical resistivity, (b) bulk radial TEGs performance vs electrical resistivity, (c) printed radial TEGs performance vs thermal resistivity, (d) bulk radial TEGs performance vs thermal resistivity.

editing. **David Astrain:** Writing – review & editing, Validation, Supervision. **Uli Lemmer:** Writing – review & editing, Validation, Supervision, Funding acquisition.

Declaration of competing interest

The authors declare that they have no known competing financial interests or personal relationships that could have appeared to influence the work reported in this paper.

Acknowledgments

The authors acknowledge funding from the Deutsche Forschungsgemeinschaft (DFG, German Research Foundation) under Germany's Excellence Strategy for the Excellence Cluster "3D Matter Made to Order" (EXC-2082/2-390761711), the German Federal Ministry for Economic Affairs and Climate Action through WIPANO project 03THWBW004 for financial support. The German Federal Environmental Foundation (Deutsche Bundesstiftung Umwelt - DBU), through the DBU Ph.D. scholarship program, also supported this work. This project has received funding from the European Union's Horizon 2020 Research and Innovation Program under grant agreement no. 814945—SolBio-Rev, and we acknowledge funding by the European Research Council, grant 101097876 - ORTHOGONAL. We would like to acknowledge the support of the Spanish State Research Agency and FEDER-UE under the grant PID2021-124014OB-I00.

Appendix A. Supplementary data

Supplementary data to this article can be found online at https://doi.org/10.1016/j.applthermaleng.2026.130125.

Data availability

Data will be made available on request.

References

[1] A. Fam, S. Fam, Review of the US 2050 long term strategy to reach net zero carbon emissions, Energy Rep. 12 (2024) 845–860, https://doi.org/10.1016/j.egyr.2024.06.031.
[2] B. Anya, M. Mohammadpourfard, G.G. Akkurt, B. Mohammadi-Ivatloo, Exploring geothermal energy based systems: review from basics to smart systems, Renew. Sust. Energ. Rev. 210 (2025) 115185, https://doi.org/10.1016/j.rser.2024.115185.
[3] G.M. Idroes, M. Afjal, M. Khan, M. Haseeb, I. Hardi, T.R. Noviandy, R. Idroes, Exploring the role of geothermal energy consumption in achieving carbon neutrality and environmental sustainability, Heliyon 10 (2024) e40709, https://doi.org/10.1016/j.heliyon.2024.e40709.
[4] M. Alsaleh, Z. Yang, T. Chen, X. Wang, A.S. Abdul-Rahim, H. Mahmood, Moving toward environmental sustainability: assessing the influence of geothermal power on carbon dioxide emissions, Renew. Energy 202 (2023) 880–893, https://doi.org/10.1016/j.renene.2022.11.060.
[5] G.M. Idroes, I. Hardi, I.S. Hilal, R.T. Utami, T.R. Noviandy, R. Idroes, Economic growth and environmental impact: assessing the role of geothermal energy in developing and developed countries, Innov. Green Dev. 3 (2024) 100144, https://doi.org/10.1016/j.igd.2024.100144.
[6] A. Aprianto, A. Maulana, T.R. Noviandy, A. Lala, M. Yusuf, M. Marwan, R.P. F. Afidh, I. Irvanizam, N. Nizamuddin, G.M. Idroes, Exploring geothermal manifestations in Ie Jue, Indonesia: enhancing safety with unmanned aerial vehicle, Leuser, J. Environ. Stud. 1 (2023) 47–54, https://doi.org/10.60084/ljes.v1i2.75.
[7] M. Tuschl, T. Kurevija, Defining heat in place for the discovered geothermal brine reservoirs in the Croatian part of Pannonian Basin, Water 15 (2023) 1237, https://doi.org/10.3390/w15061237.
[8] J. Terrapon-Pfaff, C. Dienst, J. König, W. Ortiz, A cross-sectional review: impacts and sustainability of small-scale renewable energy projects in developing countries, Renew. Sust. Energ. Rev. 40 (2014) 1–10, https://doi.org/10.1016/j.rser.2014.07.161.
[9] A. Raihan, S. Farhana, D.A. Muhtasim, M.A.U. Hasan, A. Paul, O. Faruk, The nexus between carbon emission, energy use, and health expenditure: empirical evidence from Bangladesh, Carbon Res. 1 (2022) 30, https://doi.org/10.1007/s44246-022-00030-4.
[10] T. Ding, J. Liu, K. Shi, S. Hu, H. Yang, Theoretical study on geothermal power generation using thermoelectric technology: a potential way to develop geothermal energy, Int. J. Green Energy 18 (2021) 297–307, https://doi.org/10.1080/15435075.2020.1854271.
[11] D.W. Brown, D.V. Duchane, G. Heiken, V.T. Hriscu, Mining the Earth's Heat: Hot Dry Rock Geothermal Energy, Springer Berlin Heidelberg, Berlin, Heidelberg, 2012, https://doi.org/10.1007/978-3-540-68910-2.
[12] S. Ganguly, M.S.M. Kumar, Geothermal reservoirs – a brief review, J. Geol. Soc. India 79 (2012) 589–602, https://doi.org/10.1007/s12594-012-0098-8.
[13] P. Alegria, L. Catalan, M. Araiz, A. Rodriguez, D. Astrain, Experimental development of a novel thermoelectric generator without moving parts to harness shallow hot dry rock fields, Appl. Therm. Eng. 200 (2022) 117619, https://doi.org/10.1016/j.applthermaleng.2021.117619.
[14] Z.H. Khan, H. Xie, L. Sun, W. Yang, W.A. Khan, B. Li, X. Long, J. Wang, C. Li, M. Gao, H. Ruan, Optimized thermoelectric generation for efficient low-medium temperature geothermal energy harvesting, Renew. Energy 239 (2025) 122032, https://doi.org/10.1016/j.renene.2024.122032.
[15] P. Alegría, L. Catalán, M. Araiz, I. Erro, D. Astrain, Design and optimization of thermoelectric generators for harnessing geothermal anomalies: a computational model and validation with experimental field results, Appl. Therm. Eng. 236 (2024) 121364, https://doi.org/10.1016/j.applthermaleng.2023.121364.
[16] D.M. Rowe, Thermoelectrics Handbook: Macro to Nano, CRC Press, 2005.
[17] M. Hekim, E. Cetin, Energy analysis of a geothermal power plant with thermoelectric energy harvester using waste heat, Int. J. Energy Res. 45 (2021) 20891–20908, https://doi.org/10.1002/er.7145.
[18] C. Suter, Z. Jovanovic, A. Steinfeld, A 1 kWel thermoelectric stack for geothermal power generation - Modeling and geometrical optimization, Thessaloniki, Greece, 2012, pp. 540–543, https://doi.org/10.1063/1.4731613.
[19] C. Liu, P. Chen, K. Li, A 500 W low-temperature thermoelectric generator: design and experimental study, Int. J. Hydrog. Energy 39 (2014) 15497–15505, https://doi.org/10.1016/j.ijhydene.2014.07.163.
[20] R. Ahiska, H. Mamur, Design and implementation of a new portable thermoelectric generator for low geothermal temperatures, IET Renew. Power Gen. 7 (2013) 700–706, https://doi.org/10.1049/iet-rpg.2012.0320.
[21] E. Gholamian, A. Habibollahzade, V. Zare, Development and multi-objective optimization of geothermal-based organic Rankine cycle integrated with thermoelectric generator and proton exchange membrane electrolyzer for power and hydrogen production, Energy Convers. Manag. 174 (2018) 112–125, https://doi.org/10.1016/j.enconman.2018.08.027.
[22] S. Khanmohammadi, M. Saadat-Targhi, F.W. Ahmed, M. Afrand, Potential of thermoelectric waste heat recovery in a combined geothermal, fuel cell and organic Rankine flash cycle (thermodynamic and economic evaluation), Int. J. Hydrog. Energy 45 (2020) 6934–6948, https://doi.org/10.1016/j.ijhydene.2019.12.113.
[23] L. Catalan, M. Araiz, P. Aranguren, G.D. Padilla, P.A. Hernandez, N.M. Perez, C. Garcia De La Noceda, J.F. Albert, D. Astrain, Prospects of autonomous volcanic monitoring stations: experimental investigation on thermoelectric generation from fumaroles, Sensors 20 (2020) 3547, https://doi.org/10.3390/s20123547.
[24] L. Catalan, P. Aranguren, M. Araiz, G. Perez, D. Astrain, New opportunities for electricity generation in shallow hot dry rock fields: a study of thermoelectric generators with different heat exchangers, Energy Convers. Manag. 200 (2019) 112061, https://doi.org/10.1016/j.enconman.2019.112061.
[25] L. Catalan, M. Araiz, P. Aranguren, D. Astrain, Computational study of geothermal thermoelectric generators with phase change heat exchangers, Energy Convers. Manag. 221 (2020) 113120, https://doi.org/10.1016/j.enconman.2020.113120.
[26] L. Catalan, P. Alegria, M. Araiz, D. Astrain, Field test of a geothermal thermoelectric generator without moving parts on the hot dry rock field of Timanfaya National Park, Appl. Therm. Eng. 222 (2023) 119843, https://doi.org/10.1016/j.applthermaleng.2022.119843.
[27] P. Alegría, L. Catalán, M. Araiz, Á. Casi, D. Astrain, Thermoelectric generator for high temperature geothermal anomalies: experimental development and field operation, Geothermics 110 (2023) 102677, https://doi.org/10.1016/j.geothermics.2023.102677.
[28] P. Alegría, N. Pascual, L. Catalán, M. Araiz, D. Astrain, 400 W facility of geothermal thermoelectric generators from hot dry rocks on the Canary Islands, Sustain. Energy Technol. Assess. 78 (2025) 104338, https://doi.org/10.1016/j.seta.2025.104338.
[29] D. Astrain, N. Pascual, L. Catalán, M. Araiz, P. Alegría, B. Rosado, M. Berrocoso, Continuous electric energy production in Antarctica through geothermal passive thermoelectric generators, Appl. Therm. Eng. 279 (2025) 127517, https://doi.org/10.1016/j.applthermaleng.2025.127517.
[30] Y. Lan, S. Wang, J. Lu, H. Zhai, L. Mu, Comparative analysis of organic rankine cycle, Kalina cycle and thermoelectric generator to recover waste heat based on energy, exergy, economic and environmental analysis method, Energy Convers. Manag. 273 (2022) 116401, https://doi.org/10.1016/j.enconman.2022.116401.
[31] D. Ji, H. Cai, Z. Ye, D. Luo, G. Wu, A. Romagnoli, Comparison between thermoelectric generator and organic Rankine cycle for low to medium temperature heat source: a techno-economic analysis, Sustain. Energy Technol. Assess. 55 (2023) 102914, https://doi.org/10.1016/j.seta.2022.102914.
[32] C.B. Vining, An inconvenient truth about thermoelectrics, Nat. Mater. 8 (2009) 83–85, https://doi.org/10.1038/nmat2361.
[33] A.G. Rösch, L. Franke, M.M. Mallick, U. Lemmer, Optimizing printed thermoelectric generators with geometry and processibility limitations, 2023, https://doi.org/10.5445/IR/1000156007.
[34] L. Franke, A. Georg Rösch, M.I. Khan, Q. Zhang, Z. Long, I. Brunetti, M.N. Joglar, A. M. Lara, C.D. Simão, H. Geßwein, A. Nefedov, Y.M. Eggeler, U. Lemmer, M. M. Mallick, High power density Ag_2 se/$Sb_{1.5}$ $Bi_{0.5}$ Te_3 -based fully printed origami

thermoelectric module for low-grade thermal energy harvesting, Adv. Funct. Mater. 34 (2024) 2403646, https://doi.org/10.1002/adfm.202403646.
[35] S. Antharam, M.I. Khan, L. Franke, Z. Wang, N. Luo, J. Feßler, W. Xie, U. Lemmer, M.M. Mallick, Milliwatt-scale 3D thermoelectric generators *via* additive screen printing, Energy Environ. Sci. 18 (2025) 7648–7659, https://doi.org/10.1039/D5EE01151E.
[36] M.I. Khan, L. Franke, A.G. Rösch, Md. Mofasser Mallick, U. Lemmer, Design and optimization of printed thermoelectric generators for integration into plate heat exchangers in district heating applications, Energy Convers. Manag. 334 (2025) 119834, https://doi.org/10.1016/j.enconman.2025.119834.
[37] K. Yazawa, A. Shakouri, Optimization of power and efficiency of thermoelectric devices with asymmetric thermal contacts, J. Appl. Phys. 111 (2012) 024509, https://doi.org/10.1063/1.3679544.
[38] D. Astrain, J.G. Vián, A. Martínez, A. Rodríguez, Study of the influence of heat exchangers' thermal resistances on a thermoelectric generation system, Energy 35 (2010) 602–610, https://doi.org/10.1016/j.energy.2009.10.031.
[39] F.P. Incropera, D.P. DeWitt, Fundamentals of Heat Transfer, Wiley, New York, 1981.
[40] C. Goupil (Ed.), Continuum Theory and Modeling of Thermoelectric Elements, Wiley-VCH Verlag GmbH & Co. KGaA, Weinheim, Germany, 2016.
[41] Y. Zhao, X. Zhao, M. Tian, W. Wang, S. Wang, H. Wei, M. Ge, A review of heat pipe thermoelectric generators: principles, applications, and challenges, Sol. Energy 300 (2025) 113850, https://doi.org/10.1016/j.solener.2025.113850.
[42] T. Pujol, I. T'Jollyn, E. Massaguer, A. Massaguer, I.R. Cózar, M. De Paepe, Design optimization of plate-fin heat sink with forced convection for single-module thermoelectric generator, Appl. Therm. Eng. 221 (2023) 119866, https://doi.org/10.1016/j.applthermaleng.2022.119866.
[43] D. Astrain, J. Jaramillo-Fernandez, M. Araiz, A. Francone, L. Catalán, A. Jacobo-Martín, P. Alegría, C.M. Sotomayor-Torres, Enhanced behaviour of a passive thermoelectric generator with phase change heat exchangers and radiative cooling, Appl. Therm. Eng. 225 (2023) 120162, https://doi.org/10.1016/j.applthermaleng.2023.120162.
[44] A. Elghool, F. Basrawi, H. Ibrahim, T. Ibrahim, Investigation on the performance of a prototype of thermo-electric generation with heat pipe-heat sink, MATEC Web Conf. 131 (2017) 01005, https://doi.org/10.1051/matecconf/201713101005.
[45] A. Elghool, F. Basrawi, T.K. Ibrahim, K. Habib, H. Ibrahim, D.M.N.D. Idris, A review on heat sink for thermo-electric power generation: classifications and parameters affecting performance, Energy Convers. Manag. 134 (2017) 260–277, https://doi.org/10.1016/j.enconman.2016.12.046.
[46] A. Elghool, F. Basrawi, H. Ibrahim, T.K. Ibrahim, M. Ishak, T.M. Yusof, S. A. Bagaber, Enhancing the performance of a thermo-electric generator through multi-objective optimisation of heat pipes-heat sink under natural convection, Energy Convers. Manag. 209 (2020) 112626, https://doi.org/10.1016/j.enconman.2020.112626.
[47] A. Elghool, F. Basrawi, T.K. Ibrahim, H. Ibrahim, M. Ishak, M. Hazwan Bin Yusof, S. A. Bagaber, Multi-objective optimization to enhance the performance of thermo-electric generator combined with heat pipe-heat sink under forced convection, Energy 208 (2020) 118270, https://doi.org/10.1016/j.energy.2020.118270.
[48] A. Elghool, F. Basrawi, H. Ibrahim, T.K. Ibrahim, S.A. Sulaiman, M. Ishak, Study on the performance of a thermo-electric generation model with two different materials of heat pipe-heat sink, MATEC Web Conf. 225 (2018) 04009, https://doi.org/10.1051/matecconf/201822504009.
[49] M.M. Mallick, L. Franke, A.G. Rösch, H. Geßwein, Z. Long, Y.M. Eggeler, U. Lemmer, High figure-of-merit telluride-based flexible thermoelectric films through interfacial modification via millisecond photonic-curing for fully printed thermoelectric generators, Adv. Sci. 9 (2022) 2202411, https://doi.org/10.1002/advs.202202411.